ADVANCED MATERIALS TECHNOLOGIES
www.advmattechnol.de

Self-Calibrated Flexible Holographic Curvature Sensor

*Jianling Xiao, Tomasz Plaskocinski, Mohammad Biabanifard, and Andrea Di Falco**

Optical curvature sensors find regular use in deformation analysis, typically requiring pre-calibration and post-processing of the gathered data. In this work, a self-calibrated curvature sensor based on flexible holographic metasurfaces operating in the visible range is presented. In contrast to existing solutions, the sensor can be fabricated independently from the target objects and provides an immediate readout of their curvature. The sensor consists of distinct patterned areas that create images of a reference scale and of a position indicator, which shift with respect to each other, as the metasurface is deformed. The results of this sensor are validated with an external calibration and critically discuss the types of deformations that the sensor can detect. This feature makes the sensor particularly attractive for applications where real-time curvature monitoring is essential, such as in robotics, biomechanics, and structural health monitoring.

1. Introduction

Optical curvature sensors are practical tools for measuring the mechanical deformation of objects and surfaces.[1,2] They offer angular detection with high resolution, making them an excellent candidate for integration with curvature-sensitive applications such as soft-bodied robots[3,4] and optical fibers.[5] External curvature sensors often rely on interferometry[6-8] to detect the interference fringes from the object and a reference beam, making them suitable for non-contact measurement methods. However, they typically require high beam coherence, which limits their range, precise alignment, and time-consuming measurements.[9] When embedded in fibers, curvature sensors use either photonic crystals,[10,11] Bragg gratings,[12-14] or long-period diffraction gratings[15,16] with a known lattice constant, and extract information on the curvature by tracking the intensity or wavelength of the spectral features of the transmitted or reflected light.[17] Alternatively, curvature sensors that track the light scattered by diffraction gratings can be realized on thick flexible substrates.[18,19] In all these cases, the measurement involves converting the optical signal into an electrical one, using photodetectors or optical spectrum analyzers, which require calibration, and readout terminals to convey the data to the user.[17,20,21]

Holographic metasurfaces (HMSs) offer unique advantages in optical imaging applications, including multi-color and three-dimensional displays,[22] virtual reality,[23] augmented reality,[24] and multi-information encoding and display.[25,26] These advantages stem from their ability to manipulate the properties of light, such as phase,[27] amplitude,[28] and polarization.[29] The precise wavefront control is enabled by arranging the meta-atoms in sub-wavelength scale arrays to generate intricate interference patterns, which form the target holographic images over a wide range of wavelengths, from visible to ultraviolet.[30,31] HMSs can also be applied on an extremely thin flexible substrate and thus provide more functional applications in the real world. They are conformable and can be transferred to non-flat substrates for multiplexing and imaging applications.[32-35] These properties make HMSs an excellent candidate for curvature sensing applications.

In this paper, we present a flexible self-calibrated holographic curvature sensor, operating in the visible range, designed to detect the deformation of the target object. At variance with other approaches, our sensor does not require the mapping of a given observable onto the curvature of the substrate. The holographic image instead embeds both a reference scale and an indication cursor that gives an immediately accessible readout. As shown in **Figure 1**, the target image consists of a two-dimensional (2D) scale and a dot as the curvature indicator. The position of the dot changes as the substrate deforms, with the displacement being proportional to the angle.

In the following, we present the design, fabrication, and validation of the curvature sensor. The accuracy of the self-calibration was verified independently by measuring the angle of the light reflected from a uniform area of the sensor.

2. Modeling

The phase profiles for the holograms of the 2D scale and the indicator were generated independently, using the Gerchberg-Saxton algorithm. This is in an iterative method that calculates the phase profile of a computer-generated hologram (CGH), that produces a pre-determined holographic image. Here, we use the Rayleigh-Sommerfeld integral to propagate the light between the CGH plane and the holographic image plane.[36] In this case, the sensor

J. Xiao, T. Plaskocinski, M. Biabanifard, A. Di Falco
School of Physics and Astronomy
University of St Andrews
North Haugh, St Andrews KY16 9SS, UK
E-mail: adf10@st-andrews.ac.uk

The ORCID identification number(s) for the author(s) of this article can be found under https://doi.org/10.1002/admt.202301851

DOI: 10.1002/admt.202301851

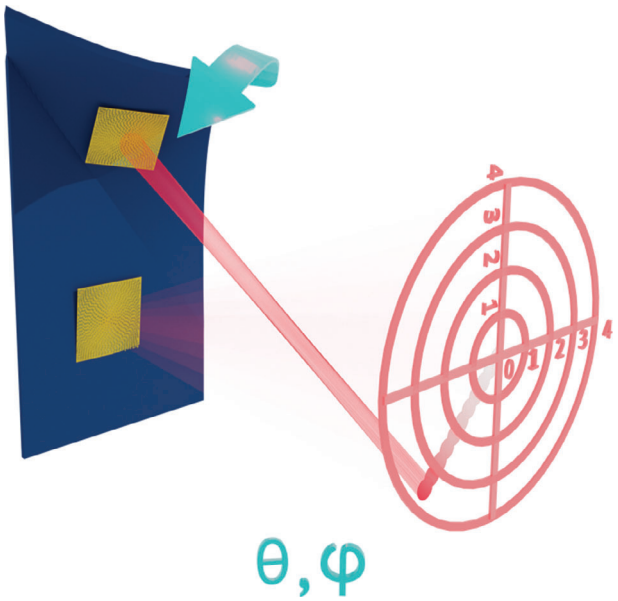

Figure 1. Concept image of the flexible curvature sensor. The two patterned areas (in gold) indicate the HMSs that generate the 2D scale image and the dot indicator image. The dot position walks across the 2D scale when the patterned areas are displaced with respect to each other. The labels on the scale are mapped to the displacement angles θ and φ.

consists of two distinct holographic images (the 2D scale and the dot indicator), projected at a defined distance from the CGH on a suitable detection surface (e.g., a diffusive screen or a wall). At this distance, the two reflected images, which propagate off-axis with respect to the incident light, converge to form the scale and the indicator. In this application, we assume that the patterned areas of the HMS undergo rigid rotations with negligible translation. We will address the effect of these approximations in the discussion section.

In this implementation, the distance between the screen and the sensor is 10 cm. The 2D scale consists of four concentric circles spaced regularly with a total diameter of 8 cm. The diameter of the indicator dot is 0.5 cm. The shape of the scale was chosen to allow for the substrate curvature to be measured in two directions along the X and Y axes. For a flat configuration (infinite radius of curvature), the sensor displays the dot in the center of the concentric circles. The patterned area that generates the indicator is positioned 1 cm away along the Y-axis from the hologram that generates the scale. This was chosen to simplify the experimental validation of the sensor, as further discussed below. Each patterned area is 300 μm × 300 μm with a resolution of 750 × 750 pixels. The 2D scale has a projection angle of $\alpha = 42°$ and off-axis angles $\theta_0 = 23.8°$ and $\varphi_0 = 18.1°$ along the X and Y axes, respectively, as shown in **Figure 2**. As the upper patterned area that encodes the dot indicator rotates with respect to the patterned area for the 2D scale, the indicator position changes, e.g. from position O to position R, within the scale. The rotation of the upper HMS along the X and Y axes to the X' and Y' axes is denoted by the angles θ and φ, respectively, as indicated in the inset. The points M and N indicate the coordinates of R on the X-axis and Y-axis, respectively.

The phase profiles of the target images are mapped onto HMSs using a 12-phase level, with a well-known metal-insulator-metal Pancharatnam-Berry meta-atoms, providing a 2π phase coverage,[37,38] for circularly polarized light. This is not a strict requirement, and other types of meta-atoms can be used, to work with linearly or unpolarized light. The unit cell, which has a periodicity of P = 400 nm, is shown as an inset of Figure S1 in the Supporting Information. The electromagnetic response of the nano-rods was simulated using computer simulation technology (CST).

3. Fabrication

The fabrication process is illustrated in **Figure 3**a–f. A silicon carrier was spin-coated with a 100 nm thick sacrificial layer (Omnicoat, Microchem), followed by a 6 μm thick SU8 polymer (Microchem) which acted as a flexible substrate. The polymer was then flood-exposed with UV light and cross-linked with a hard bake step at 170 °C for 30 min. A layer of 150 nm gold with 10 nm of NiCr as an adhesion layer was deposited via an electron beam evaporator to act as a back reflector. A 160 nm thick spacer layer of Ma-N 2403 (Micro Resist Technology) was spin-coated on the gold layer. The meta-atoms of the HMSs were defined by electron beam lithography (EBL) at a dose of 250 μC cm^{-2}. The sample was developed in Ma-D (Micro Resist Technology) and a 40 nm thick top gold cap was deposited by electron beam evaporation. At last, the flexible SU8 membrane was released from the carrier by immersing the sample in MF319 (Microposit). To facilitate the lift-off and transfer process of the sensor, we applied dicing tape to the four edges of the sample before immersing it in MF319. This prevented the released membrane from curling or folding after detachment from the silicon substrate. The released membrane was then transferred to the target substrate (e.g., a plastic film), with the help of a few drops of water, to facilitate the positioning of the sensor. The tape was finally peeled off from the membrane and the water was allowed to evaporate. In most cases, this guaranteed a strong adhesion between the membrane and the substrate. If required, an intermediate adhesive layer could be placed on the membrane. Figure 3g shows the membrane transferred on a plastic film, where the position of two distinct patterned areas is highlighted with two red dashed circles. Figure 3h is the scanning electron microscope (SEM) image of the fabricated sample. The lift-off process does not affect the quality of the HMSs, which can be confirmed by comparing the SEM images of the fabricated sample before and after lift-off, as shown in Figure S2 in the Supporting Information.

4. Characterization

To calibrate and characterize the rotation angle of the HMS and the corresponding position of the indicator on the 2D scale we used the set-up illustrated in **Figure 4**a. A linearly polarized laser beam with wavelength $\lambda = 650$ nm was expanded, collimated, and focused with lenses F1, F2, and F3 with focal lengths of 50 mm, 400 mm, and 1000 mm, respectively. The beam was divided into two arms, using two beam splitters (BSs), to illuminate both areas in the HMS. To achieve circular polarization, a $\lambda/4$ waveplate was positioned right before the sample. Due to the size differences between the 2D scale and the indicator, a $\lambda/2$ waveplate

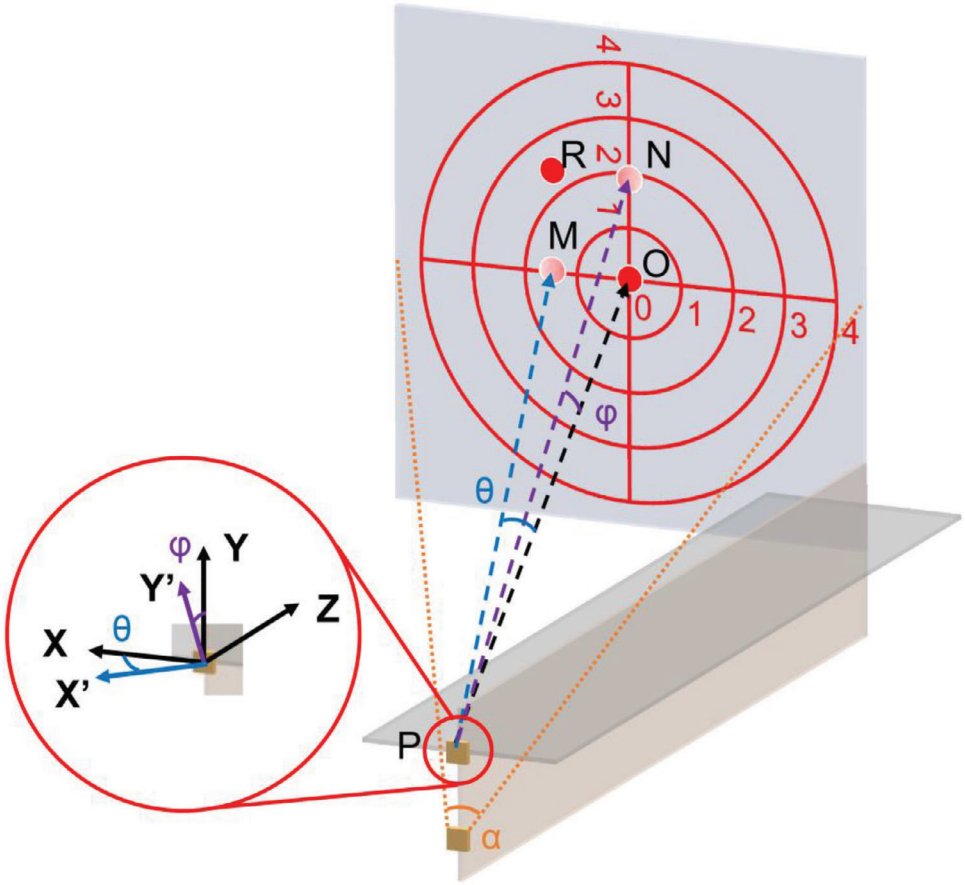

Figure 2. Schematic image of the geometric parameters of the projected image of the HMSs. The point P indicates the position of the upper patterned area, which produces the dot image. For the un-deformed configuration, the dot is projected on the O point of the scale image. The point R marks the coordinates of the dot when deformation is applied, with M and N representing the coordinates of R along the X-axis and Y-axis, respectively. θ and φ are the rotation angles of the upper region of the HMS along the X-axis and Y-axis, corresponding to the angles between $\vec{PM}$ and $\vec{PO}$, and between $\vec{PN}$ and $\vec{PO}$, respectively.

was placed before the first (polarized) BS to adjust the intensity of light incident on the two patterned areas for better contrast.

The sample was mounted on a stage composed of two parts. The upper part included a gimbal mount equipped with two motorized actuators (referred to as A and B) to rotate the top part of the HMS (for the indicator) with respect to its bottom part (for the scale). The sensor was mounted to have the patterned area for the indicator at the center of the actuated gimbal mount, to minimize the displacement upon rotation. The inset image in Figure 4a illustrates the mounting configuration of the sample on a plastic film with two laser beams incident on both patterned areas.

The holographic images were projected onto a diffusing semi-transparent board positioned at the designed distance. Figure 4b–d displays the holographic images of the 2D scale, the indicator, and both the 2D scale and the centered indicator, respectively.

5. Results and Discussion

In the following, we refer to the linear actuators controlling the rotation angles φ and θ of the HMS as A (Y-axis) and B (X-axis). To achieve different rotation angles, the travel distances ΔL_A and ΔL_B were varied in the range of $\pm$ 3 mm relative to the center position, with steps of 0.5 mm. This produced rotation angles φ and θ in the range of $\pm$ 12° with a resolution of 2°. The holographic images projected on the diffusing board were recorded by a charge-coupled device (CCD) camera. The images are slightly distorted, due to the setup constraints that require placing the CCD camera at a slight angle with respect to the board. We therefore corrected the distortion with image processing software, using the 2D scale as a guide, and extracted the coordinates of the indicator from the corrected images.

The rotation angles θ and φ were calculated by the following equations:

$$\cos\theta = \vec{PO} \cdot \frac{\vec{PM}}{|\vec{PO}||\vec{PM}|} \quad (1)$$

$$\cos\varphi = \vec{PO} \cdot \frac{\vec{PN}}{|\vec{PO}||\vec{PN}|} \quad (2)$$

where P is the center of the upper HMS and O is the center of 2D scale (see Figure 2).

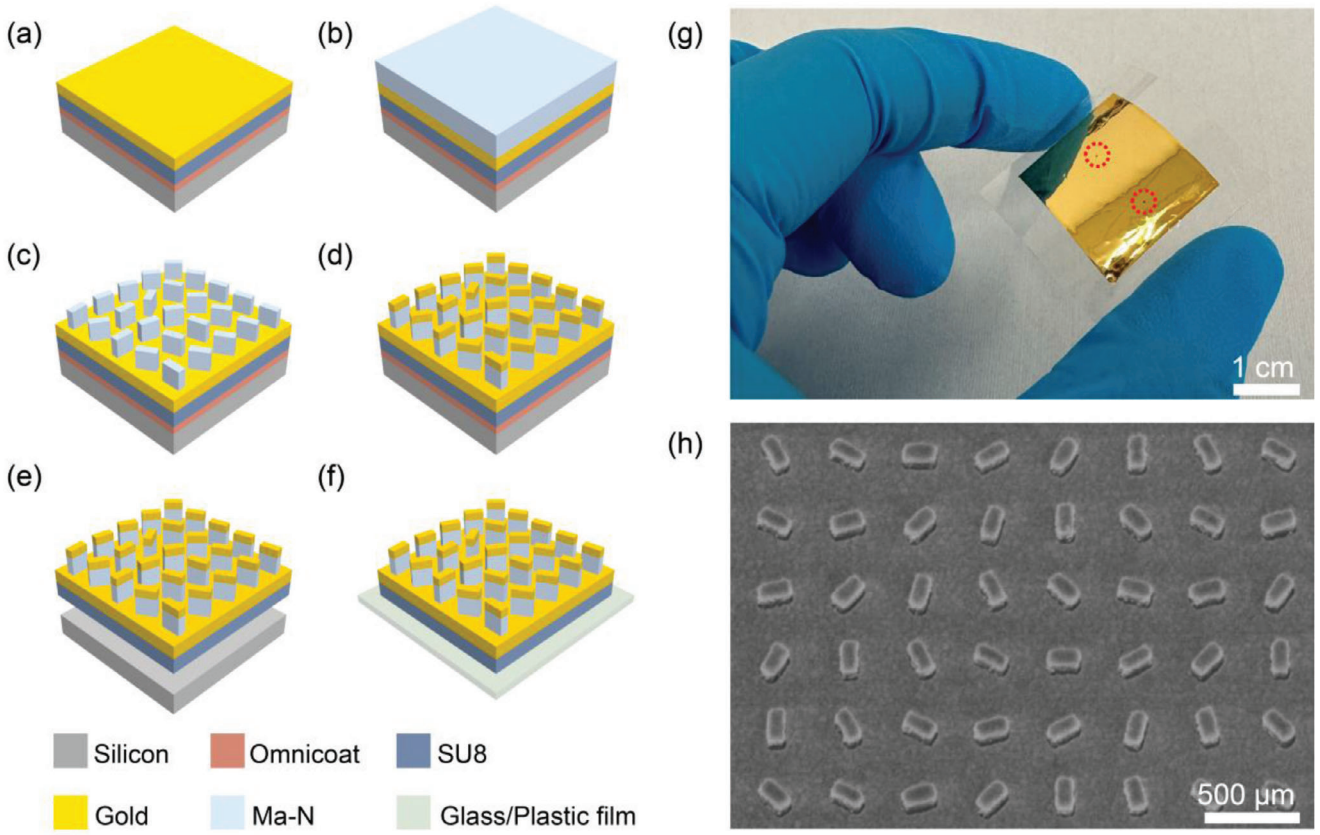

Figure 3. Sensor fabrication process. a) Spin-coating of Omnicoat, the SU8 layer, and evaporating NiCr and gold films on the silicon wafer. b) Spin-coating of Ma-N 2403 resist. c) EBL writing to define nano-rods. d) Evaporating a gold cap on top. e) Lift-off process by etching the Omnicoat layer. f) Transferring the flexible sample to a target substrate. g) Image of the HMSs transferred to a plastic film. The red dashed circles indicate the regions with the patterned areas. h) SEM image of the HMSs.

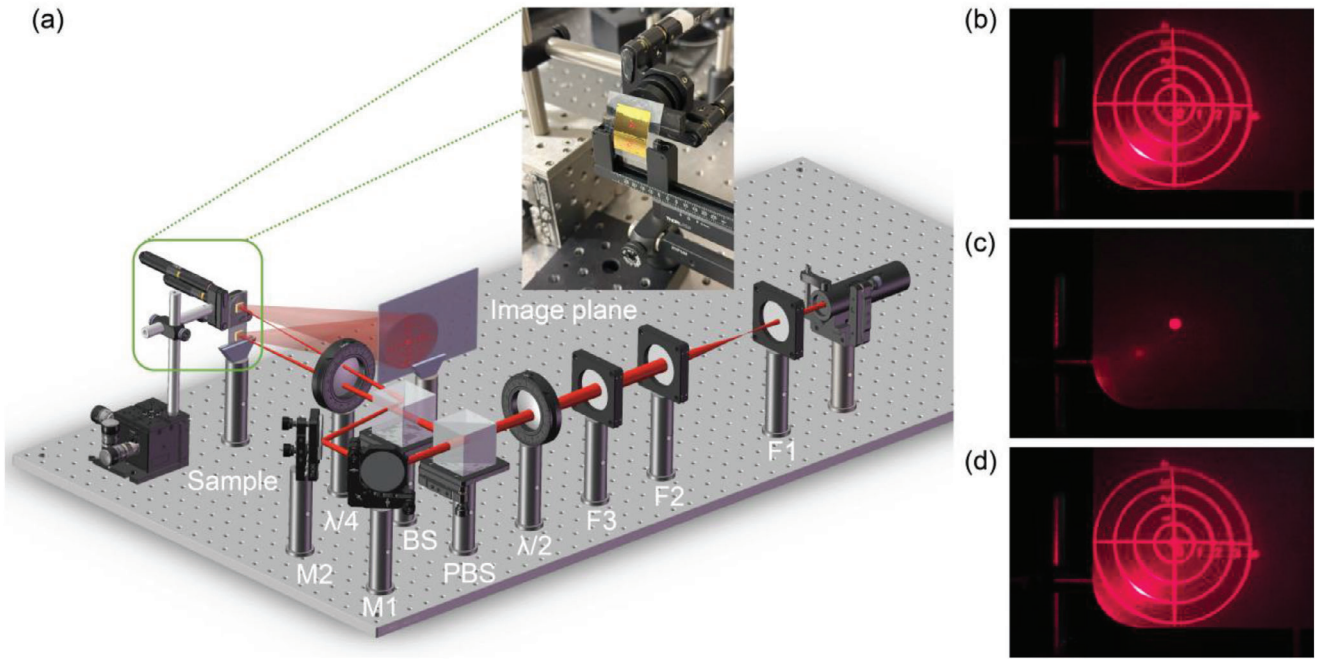

Figure 4. a) Schematic of the set-up with an image of a sample mounted on the rotation stage as an inset in the upper right. The experimental holographic images of b) 2D scale, c) indicator, and d) a combination of 2D scale with the indicator in the center.

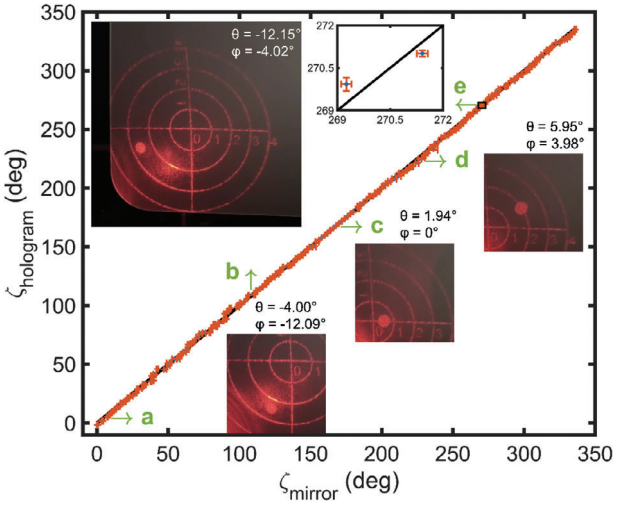

Figure 5. Plot of $\zeta_{hologram}$ versus ζ_{mirror}. The insets a–d) show the holographic images at the selected points. Inset (e) shows a zoomed-in view of the plot, highlighting the correspondence between the two methods (dots in blue), the associated uncertainty (error bars in orange), and the linear fit (continuous line in black).

In this example, the labels of the 2D scale indicate the displacement of the dot indicator in centimeters, with respect to the flat configuration. From simple geometrical consideration (see also Figure S3 in the Supporting Information) the rotation angle θ around the Y axis can be obtained with the expression

$$\tan\theta = \frac{x}{d\tan^2\theta_0 + x\tan\theta_0 + d} \tag{3}$$

where d is the distance between the HMS and the image plane, x is the displacement of the dot indicator and θ_0 is the off-axis angle. Therefore, for this specific configuration, a displacement of 1 cm along the X-axis corresponds to a rotation $\theta = 4.6°$. The same considerations can be made for rotations around the X-axis.

To validate the accuracy of the sensor, we performed an independent calibration of the curvature of the object by collecting the angle of the beam reflected from an un-patterned area. The calibrated rotation angles fit is shown in Figure S4a,b (Supporting Information) for the HMS and c, d for the reflective mirror.

For both characterization methods, the coordinates were recorded three times to estimate the uncertainty of the measurements.

To compare the two methods, we mapped the 13 × 13 grid of sampled angles onto a one-dimensional (1D) linear variable $\zeta(n) = (\theta_n+12) + 13 \times (\varphi_n+12)$, where n counts from 1 to 169. This choice allows us to directly compare the accuracy of two characterization methods. **Figure 5** shows the plot of $\zeta_{hologram}$ versus ζ_{mirror}, with the associated experimental uncertainty, where $\zeta_{hologram}$ and ζ_{mirror} are the 1D mapping variables for the hologram and the mirror methods, respectively. To construct these variables, we used the angles θ_n and φ_n obtained independently for each case. For a correctly functioning sensor, the two variables must assume the same value, and plotting one against the other must give a straight line (shown in black in Figure 5), as is the case here. The measured accuracies were 0.3° and 0.6° for the HMS and mirror cases, respectively. In both cases, the estimation of the accuracy is limited by the ability to impose a specific angle using the actuators and by the alignment of the laser with the pivot of the rotation. In other words, the accuracy of the sensor is superior to that of the validation method. The insets of Figure 5 show the images relative to the points (a-d). The inset relative to point (e) shows a zoomed-in view of the plot, where the black line is the linear fit, going through the origin of the graph, and the data are shown in blue dots with error bars in orange. The resolution and the measurable range of angles of the sensor depend on the size of the projected image . Larger images, projected at longer distances from the sensor increase its resolution. This however tends to reduce the range of angle, since it becomes more challenging to capture larger and larger images.

Since the images of the 2D scale and indicator overlap correctly only on the imaging plane, we explored the dependency of the measurement accuracy on the relative position of the detection screen.

To simplify, we tested this dependency in the flat sensor case. As expected, the size of both images is magnified as the distance of the observation plane increases, while the position of the indicator walks across the 2D scale, passing through the central position at the designed distance. Tilting the diffusive board with respect to the ideal imaging plane produces distorted images, with a less pronounced effect on the position of the indicator on the scale. Figure S5 and Table S1 (Supporting Information) show these results quantitatively. It should be noted that the specific tolerances with respect to misalignments of the imaging plane are strongly correlated to the ratio between the distance of the screen from the HMS and the separation between the patterned areas relative to the indicator and to the scale on the HMS. For larger ratios, the parallax is reduced and so are the effects of possible misalignments. On the other hand, the notion that the indicator and the scale are aligned by design in the flat case can be used to establish the accurate positioning of the observation screen before the measurement of deformations.

It is important to highlight that both the scale and the indicator design can be tailored to a variety of different configurations. In this case, we placed the patterned areas in the HMS related to the scale and to the indicator at a distance that would facilitate the validation of the sensor.

On the side of the HMSs, for example, it would be straightforward to increase the number and density of the patterned areas, to map the local distortion and curvature across the whole surface, rather than that of one point with respect to another one, as we did here. Likewise, on the imaging side, different strategies can be adopted, e.g., creating local scales and indication points to relay the local distortions directly to the observer, including using a scale with angles labeled in the image itself. Additionally, the illumination of the sensor could be done with a single, uniform source, instead of using two smaller laser beams. These choices determine key aspects of the sensor, including its resolution, the range of measured angles, and the tolerance to misalignments between the HMSs and the imaging surface.

In this case, we assumed that the minimum radius of curvature of the membrane is larger than the patterned areas, which are therefore assumed to be undistorted. Typically, for a radius of curvature 30% greater than the length of the patterned area, the normalized correlation of the holographic image with the image of the undistorted case is better than 3 dB.[36] For our sensor, this

means that a readable image can be formed down to a radius of curvature of 0.5 mm, at the cost of an increasingly compromised accuracy. However, this is not an intrinsic limitation of the platform and can be easily removed. If desired, the curvature of the patterned areas can be used directly to extract information on the topology of the deformation at small scales, thus providing the sensor with additional degrees of freedom.[35,36]

As typical of out-of-plane optical curvature sensors (e.g., based on diffraction gratings), the resolution of our approach is not limited by the ability to resolve narrow spectral features, as for optical fiber-based sensors. On the other hand, since our sensor measures the relative rotation of two points on a surface it is less capable of producing large-scale and spatially resolved images of complex deformations than interferometric methods. However, within the limit of a local detection, our sensor offers comparable resolution, without requiring optical sources with long coherence lengths. This versatility, coupled with the ability to relay the readout without pre-calibration and further analysis, marks the main difference between our sensor and alternative solutions. Additionally, contrarily to embedded sensors, our device can be applied to existing devices or materials, independently from their manufacturing and operational requirements.

6. Conclusion

In this paper, we demonstrated the design, fabrication, and characterization of a self-calibrated flexible holographic metasurface curvature sensor. The sensor was designed to work in the visible range, where the curvature is directly revealed by the position of an indicator with respect to an intrinsically aligned scale. The demonstration of the self-calibrated flexible holographic curvature sensor is of particular interest for applications where it can be applied after the fabrication of the target substrate, without impacting its motion, and where an immediate readout of the curvature is required. A meaningful example is that of soft robots and wearable sensing applications, where machine-human interactions require direct and simplified feedback on the status of the sensor.

Supporting Information

Supporting Information is available from the Wiley Online Library or from the author.

Acknowledgements

The authors acknowledge support from the EPSRC. The project was supported by the European Research Council (ERC) under the European Union Horizon 2020 research and innovation program (Grant Agreement No. 819346).

Conflict of Interest

The authors declare no conflict of interest.

Data Availability Statement

The data that support the findings of this study are openly available in University of St Andrews at [https://doi.org/10.17630/7d90ba28-cd6a-4bc5-a4e1-d5a3d7314dd6], reference number 39.

Keywords

conformable and flexible metasurfaces, curvature sensors, holographic metasurfaces

Received: October 30, 2023
Revised: December 21, 2023
Published online:

[1] C. Inneam, K. Srinuanjan, W. Yindeesuk, *J. Phys.: Conf. Series* **2021**, *2145*, 012054.
[2] D. Yu, Q. Liu, Y. He, H. Liu, S. Luo, *Opt. Laser Technol.* **2021**, *143*, 107374.
[3] S. Ozel, N. A. Keskin, D. Khea, C. D. Onal, *Sens. Actuators, A* **2015**, *236*, 349.
[4] M. Grube, R. Seifried, *Symposium on Robot Design, Dynamics and Control*, Springer International Publishing, Cham **2022**, pp. 125–132.
[5] Y. P. Li, W. G. Zhang, S. Wang, L. Chen, Y. X. Zhang, B. Wang, T. Y. Yan, X. Y. Li, W. Hu, *IEEE Photonics Technol. Lett.* **2016**, *29*, 224.
[6] A. Ali, M. Amer, N. Nada, *J. Opt.* **2023**, 1, https://doi.org/10.1007/s12596-023-01269-9
[7] W. Gong, J. Dou, Y. Hu, Z. Yang, *Opt. Laser Technol.* **2023**, *161*, 109176.
[8] Z. Yang, Z. Gao, Q. Yuan, J. Ye, M. Li, *Opt. Lasers Engin.* **2014**, *56*, 35.
[9] S. Yang, G. Zhang, *Meas. Sci. Technol.* **2018**, *29*, 102001.
[10] H. Gong, H. Song, X. Li, J. Wang, X. Dong, *Sens. Actuators, A* **2013**, *195*, 139.
[11] W. M. Guimarães, C. M. Cordeiro, M. A. Franco, J. H. Osório, *Fibers* **2021**, *9*, 72.
[12] S. Deng, T. Wang, B. Tan, W. Yu, G. Lu, *Smart Mater. Struct.* **2022**, *31*, 114001.
[13] F. Velazquez-Carreon, A. Perez-Alonzo, G. Sandoval-Romero, *Opt. Fiber Technol.* **2023**, *77*, 103257.
[14] F. Zhu, Y. Zhang, Y. Qu, W. Jiang, H. Su, Y. Guo, K. Qi, *Opt. Fiber Technol.* **2020**, *54*, 102133.
[15] J. A. Martin-Vela, J. M. Sierra-Hernandez, A. Martinez-Rios, J. M. Estudillo-Ayala, E. Gallegos-Arellano, D. Toral-Acosta, T. E. Porraz-Culebro, D. Jauregui-Vazquez, *IEEE Photonics Technol. Lett.* **2019**, *31*, 1265.
[16] H. C. Li, J. Liu, X. D. He, J. Yuan, Q. Wu, B. Liu, *IEEE Trans. Instrum. Meas.* **2023**, *72*, 7001109.
[17] Q. Wang, Y. Liu, *Measurement* **2018**, *130*, 161.
[18] G. Sun, X. Zhang, M. Dong, Y. He, M. Yu, L. Zhu, *Optik* **2019**, *177*, 26.
[19] D. Yu, Y. He, H. Liu, B. Wang, L. Li, R. Wang, S. Luo, *Opt. Lett.* **2020**, *45*, 579.
[20] S. Li, H. Zhao, R. F. Shepherd, *MRS Bull.* **2017**, *42*, 138.
[21] O. Yasa, Y. Toshimitsu, M. Y. Michelis, L. S. Jones, M. Filippi, T. Buchner, R. K. Katzschmann, *Annual Rev. Control, Robot., Autonom. Syst.* **2023**, *6*, 1.
[22] S. So, J. Kim, T. Badloe, C. Lee, Y. Yang, H. Kang, J. Rho, *Adv. Mater.* **2023**, *35*, 2208520.
[23] W. Song, X. Liang, S. Li, P. Moitra, X. Xu, E. Lassalle, Y. Zheng, Y. Wang, R. Paniagua-Domínguez, A. I. Kuznetsov, *Adv. Opt. Mater.* **2023**, *11*, 2202348.
[24] Z. Liu, D. Wang, H. Gao, M. Li, H. Zhou, C. Zhang, *Adv. Photon.* **2023**, *5*, 034001.
[25] B. Xiong, Y. Liu, Y. Xu, L. Deng, C. W. Chen, J. N. Wang, R. Peng, Y. Lai, Y. Liu, M. Wang, *Science* **2023**, *379*, 294.
[26] Y. Wang, Z. Yao, Z. Cui, G. Sun, D. Zhang, *Nanophotonics* **2023**, *12*, 4339.
[27] N. Yu, P. Genevet, M. A. Kats, F. Aieta, J. P. Tetienne, F. Capasso, Z. Gaburro, *Science* **2011**, *334*, 333.

[28] G. Y. Lee, G. Yoon, S. Y. Lee, H. Yun, J. Cho, K. Lee, H. Kim, J. Rho, B. Lee, *Nanoscale* **2018**, *10*, 4237.
[29] J. B. Mueller, N. A. Rubin, R. C. Devlin, B. Groever, F. Capasso, *Phys. Rev. Lett.* **2017**, *118*, 113901.
[30] J. Kim, W. Kim, D. K. Oh, H. Kang, H. Kim, T. Badloe, S. Kim, C. Park, H. Choi, H. Lee, *Light: Sci. Appl.* **2023**, *12*, 68.
[31] A. Asad, J. Kim, H. S. Khaliq, N. Mahmood, J. Akbar, M. T. S. Chani, Y. Kim, D. Jeon, M. Zubair, M. Q. Mehmood, *Nanoscale Horiz.* **2023**, *8*, 759.
[32] J. Burch, D. Wen, X. Chen, A. Di Falco, *Sci. Rep.* **2017**, *7*, 4520.
[33] H. S. Ee, R. Agarwal, *Nano Lett.* **2016**, *16*, 2818.
[34] S. C. Malek, H. S. Ee, R. Agarwal, *Nano Lett.* **2017**, *17*, 3641.
[35] J. Xiao, R. I. Hunter, D. A. Robertson, G. M. Smith, S. Horsley, S. A. Schulz, A. D. Falco, *Adv. Mater. Technol.* **2023**, *8*, 2202006.
[36] J. Burch, A. Di Falco, *ACS Photonics* **2018**, *5*, 1762.
[37] G. Zheng, H. Mühlenbernd, M. Kenney, G. Li, T. Zentgraf, S. Zhang, *Nat. Nanotechnol.* **2015**, *10*, 308.
[38] L. Yan, J. Xiao, T. Plaskocinski, M. Biabanifard, S. Persheyev, M. Askari, A. D. Falco, *Opt. Exp.* **2022**, *30*, 19145.
[39] J. Xiao, T. Plaskocinski, M. Biabanifard, A. Di Falco, Self-Calibrated Flexible Holographic Curvature Sensor (Dataset), 2024, University of St Andrews Research Portal, https://doi.org/10.17630/7d90ba28-cd6a-4bc5-a4e1-d5a3d7314dd6 (accessed: February 2024).